ACS APPLIED NANO MATERIALS

www.acsanm.org Article

Biomineralization of Nanocrystalline CdS/ZnS Photocatalysts via Controlled Surface Passivation for Enhanced Hydrogen Evolution

John Sakizadeh, Joseph P. Cline, Mark A. Snyder, Christopher J. Kiely, and Steven McIntosh*

Cite This: *ACS Appl. Nano Mater.* 2022, 5, 2293−2304 Read Online

ACCESS | Metrics & More | Article Recommendations | Supporting Information

ABSTRACT: The high-temperature processing and organic solvents used in the synthesis of heterojunction photocatalysts is a challenge for the large-scale manufacturing that will be necessary for impact at the societal scale. While syntheses under more benign conditions have been demonstrated, the resulting material performance is often not competitive. Herein, we demonstrate the controlled, aqueous phase, and ambient temperature biomineralization-based synthesis of nanocrystalline CdS/ZnS core/shell hydrogen evolution photocatalysts using a purified form of the enzyme, cystathionine γ-lyase. Photocatalytic hydrogen evolution measurements show that controlled Zn^{2+}-based passivation of the surface of CdS improves the hydrogen evolution activity from 1300 μmol h^{-1} g^{-1} to 3200 μmol h^{-1} g^{-1} in the presence of a Na_2S/Na_2SO_3 sacrificial reagent, which is on par with reported hydrogen evolution rates of CdS/ZnS core/shell photocatalysts synthesized through traditional chemical routes. The steady-state photoluminescence (PL) intensity and PL lifetime measurements coupled with energy-dispersive X-ray spectroscopy indicate that Zn^{2+} passivates the surface of biomineralized CdS nanocrystals, with the extent of passivation controlled by the concentration of the zinc precursor added directly to the synthesis solution. Photodeposition of a platinum cocatalyst onto the highest-performing CdS/ZnS photocatalyst further boosts the hydrogen evolution rate to 7200 μmol h^{-1} g^{-1} in the presence of a Na_2S/Na_2SO_3 sacrificial reagent, establishing biomineralization as an effective platform for the controlled synthesis of high-performing heterojunction hydrogen evolution photocatalysts.

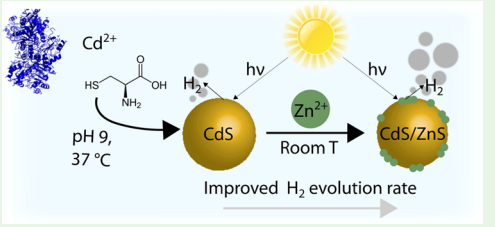

KEYWORDS: *photocatalysis, biomineralization, hydrogen generation, nanomaterials, cadmium sulfide*

INTRODUCTION

Hydrogen production through photocatalysis is a promising route to convert solar energy into chemical energy using water, an abundant resource, as a reactant. Highly efficient photocatalysts require (i) minimal overpotential to drive both the oxidative and reductive photocatalytic reactions on the surface and (ii) the suppression of charge carrier recombination. Economical large-scale utilization of these photocatalysts further requires that this efficiency is achieved using earth-abundant materials, is coupled with high stability, and that the photocatalysts themselves are manufactured using sustainable and economically viable processes.[1] Meeting all these demands with a single material is, arguably, impossible. For example, CdS nanocrystals, which are very well-studied photocatalysts for hydrogen evolution, are comprised of earth-abundant components and can be manufactured through bioinspired approaches in water at room temperature,[2,3] but when employed in their native form, they suffer from low catalytic activity and easily succumb to photocorrosion.[4]

The activity and stability of CdS nanocrystals are greatly improved through integration with another semiconductor to form a heterojunction structure.[5−7] In a type-I heterojunction core−shell system, a core nanoparticulate material is encapsulated by a shell material that has a conduction and valence band at lower and higher potentials, respectively, relative to the core material. This type-I, core−shell architecture creates a potential well that confines photogenerated charge carriers to the core material, while the shell material simultaneously passivates surface traps to increase charge carrier lifetime and protects the core material from photocorrosion.[8,9] Many reports have demonstrated that ZnS, a wide band gap semiconductor also formed from earth-abundant materials, forms a type-I heterojunction when in contact with CdS. The resulting core/shell photocatalysts exhibit substantially improved performance; Xie et al. have reported a ∼50-fold enhancement in the hydrogen evolution rate for CdS with a mesoporous ZnS shell relative to bare CdS with stability up to 60 h.[9] While the CdS/ZnS system represents a promising route toward a scalable photocatalyst, previously reported shell growth methods rely on high synthesis temperatures and are carried out in organic solvents.[8−13] Ideally, the synthesis of these core−shell photocatalysts and their integration with a suitable support

Received: November 22, 2021
Accepted: January 10, 2022
Published: January 20, 2022

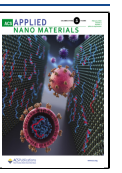

https://doi.org/10.1021/acsanm.1c03997
ACS Appl. Nano Mater. 2022, 5, 2293−2304

(e.g., reduced graphene oxide) would all occur under ambient, aqueous conditions to reduce the process energy intensity and production costs.

Aqueous, ambient temperature processes for nanomaterial synthesis have been demonstrated through biomineralization and bioinspired approaches.[14] In principle, these soft processing routes can drastically lower the environmental and economic costs of producing hydrogen evolution photocatalysts. However, the performance of bioderived photocatalysts typically lags far behind those synthesized using traditional chemical means due to the inability to achieve tight control over particle size, crystalline perfection during biosynthesis, and difficulties in postsynthetic purification of the materials from the biosynthesis medium. Yet, such control is essential for process scaleup.

We have previously demonstrated biomineralization-based synthesis of a range of highly crystalline functional metal sulfide and metal oxide nanocrystals with tight size control.[2,15−25] Specifically, for metal sulfides, we have developed a synthesis approach that utilizes the minimal set of components necessary for mineralization at room temperature in a buffered aqueous medium, namely, an active enzyme, a metal precursor, and a sulfur source. Metal sulfides are generated when a recombinant form of the enzyme cystathionine γ-lyase (CSE) turns over the amino acid L-cysteine in solution to produce dissolved HS^-, which subsequently reacts with metal ions in solution to form metal sulfide. The size control is achieved as the rate of HS^- production keeps the growth process in the size-focusing regime.[19] Herein, we demonstrate the next level of control to optimize Zn^{2+} incorporation on the native CdS particles and clearly show that biomineralization is a viable route for precisely synthesizing high-performing functional core−shell nanomaterials.

The extent of cadmium chalcogenide surface passivation by a ZnS shell is an important variable for applications requiring charge injection through the shell of core−shell materials, such as in photocatalysis using type-I systems.[26] As the extent of surface coverage increases, so does the quantum yield of the core material, indicating increased charge carrier lifetimes as a result of increasing surface passivation.[26] However, charge transfer rates from the core, through the shell, and to an external electron acceptor eventually decrease as the shell becomes too thick and presents too large of a spatial barrier for the photoexcited electron to cross.[26] These trends in charge carrier lifetime and the rate of charge transfer through an insulating shell as a function of the extent of surface passivation have been replicated in the study of photoinitiated electron transfer from a type-I $CuInS_2$/ZnS core/shell nanocrystal to a TiO_2 electron acceptor.[27] Therefore, when designing a type-I heterojunction hydrogen evolution photocatalyst, the extent of surface passivation by the shell must be precisely controlled to optimize the photoexcited charge carrier lifetime and charge transfer through the shell to the reactants. Such precise synthetic control has not previously been achieved through biomineralization routes. Herein, we investigate how the controlled and rapid deposition of Zn^{2+} onto the surface of biomineralized CdS nanocrystals under ambient temperature and aqueous conditions impacts the activity of surface-passivated CdS when employed as a hydrogen evolution photocatalyst.

RESULTS AND DISCUSSION

All-Aqueous, Ambient Synthesis of CdS/ZnS Nanocrystals. CdS nanocrystals were biomineralized using a single enzyme, CSE. CSE converts L-cysteine into HS^- in aqueous solution incubated at 37 °C, which further reacts with dissolved Cd^{2+} ions to form CdS (Scheme 1).[2] Residual L-cysteine in solution binds to the surface of the nucleating CdS species, mediating growth and stabilizing the nanocrystals.[28] Due to the constant generation of HS^- by CSE throughout the biomineralization process, the growth of the CdS nanocrystals remains in the size-focusing regime, keeping the size distribution of the nanocrystal population relatively narrow.[19] The average size of the nanocrystals was controlled by incubation time, which was set at 4 h. We have previously demonstrated that these growth conditions and incubation time yield CdS nanocrystals of ∼2−3 nm in diameter, with a characteristic UV−vis absorption peak at 390 nm (Figure 1a).[29]

Scheme 1. Depiction of the Biomineralization of CdS Nanocrystals and Subsequent Growth of a ZnS Shell through Room Temperature Addition of Zinc Acetate to the Synthesis Solution

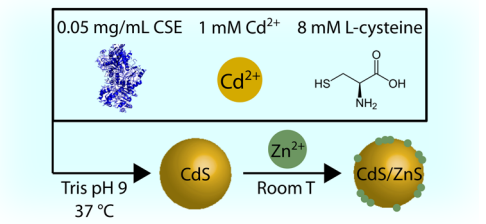

ZnS was introduced onto the core biomineralized CdS particles by the addition of controlled concentrations of zinc acetate directly to the aqueous biomineralized product solution under ambient conditions before any washing steps to remove residual HS^-, L-cysteine, and CSE. After which, the final core/shell product was precipitated by addition of ethanol, washed, and resuspended in Tris pH 9 with 8 mM L-cysteine. The increase in the peak intensity of the steady-state photoluminescence (PL) spectra (Figure 1b) with increasing concentration of zinc acetate is consistent with the formation of CdS/ZnS core−shell nanoparticles and indicates a concomitantly increasing propensity for radiative recombination of photoexcited electrons. This finding is consistent with other studies, such as that performed by Dabbousi et al., of CdSe/ZnS core−shell nanocrystals in which ZnS shell growth led to increases in the PL peak intensity.[30] In their work and further studies on CdS/ZnS, a red shift in the optical spectra accompanied ZnS shell growth was attributed to exciton leakage into the shell.[31] However, other studies report a blue shift when growing a ZnS shell on CdS and attribute this to partial alloying between the CdS and ZnS regions.[32] These conflicting reports suggest that optical properties of core−shell nanocrystals can be sensitive to specific synthesis routes and particle morphologies.

Here, the absence of optical shifts (Figure 1a) suggests that the size and composition of the CdS core remains unchanged by the addition of zinc acetate, which could be due to the low process temperatures limiting the amount of zinc incorporation into the CdS core lattice.[32,33] The extent of zinc incorporation into the core of $CuInS_2$/ZnS nanoparticles has been shown to

https://doi.org/10.1021/acsanm.1c03997
ACS Appl. Nano Mater. 2022, 5, 2293−2304

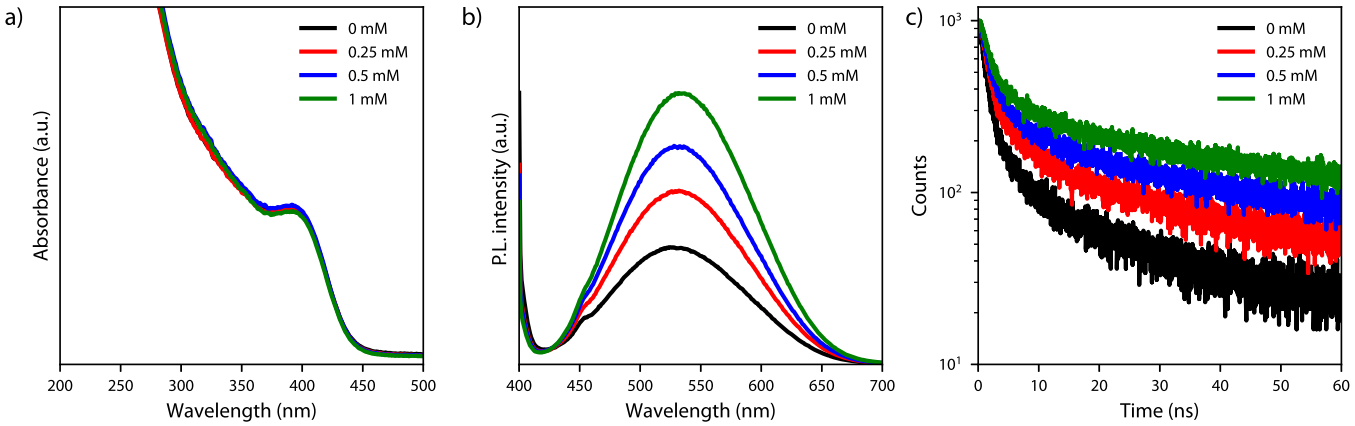

Figure 1. (a) UV−vis spectra, (b) steady-state photoluminescence spectra, and (c) time-correlated single photon counting (TCSPC) photoluminescence decay plots of CdS and CdS/ZnS nanocrystals after addition of varying specified concentrations of zinc acetate to the synthesis solution. Before spectroscopic characterization, the biomineralized CdS/ZnS was precipitated, washed, and resuspended to remove residual biomineralization components.

increase with the temperature at which the ZnS shell growth is carried out, implying that it takes place through cation exchange.[34] No additional PL peaks were observed in our case, suggesting that no secondary population of ZnS nanocrystals were formed.

Zn^{2+}-Based Surface Passivation of CdS Nanocrystals under Ambient Temperature, Aqueous Conditions. PL decay traces of the CdS/ZnS samples prepared by dosing the biomineralized CdS solutions with various concentrations of zinc acetate (Figure 1c) demonstrate an increased PL lifetime with higher concentrations of zinc acetate. The PL lifetime data for quantum dot nanocrystals, such as CdS in this study, are typically modeled using multiexponential decay functions due to inhomogeneities within the nanocrystal population and have characteristic long and short lifetime components.[35] The PL decay profiles were fitted (Figure S1) to a biexponential decay function (eq 1)

$$I(t) = a_1 e^{-t/\tau_1} + a_2 e^{-t/\tau_2} \quad (1)$$

where a_1 and a_2 are the amplitudes and τ_1 and τ_2 are the PL lifetimes associated with the fast and slow decay components, respectively. The parameters obtained from the biexponential fits are presented in Table 1. The higher concentrations of zinc acetate led to an increase in both the short and long PL lifetimes. This is accompanied by a growing dependence on the longer lifetime term, indicative of radiative recombination, with increasing zinc acetate concentration, as evidenced by the concomitant decrease in a_1 and increase in a_2. An increase in the radiative recombination rate was also observed in other reports of CdS/ZnS core−shell nanocrystals and has been attributed to the passivation of surface traps that act as nonradiative recombination centers.[32,36] In our case, the increase in the PL lifetime indicates that Zn^{2+} is incorporating at the surface of CdS, passivating surface traps. Furthermore, the experimentally obtained lifetimes in this study are consistent with those obtained in previous studies of cadmium chalcogenide/ZnS core−shell nanocrystals, 15−30 ns, and CdS/ZnS core−shell nanocrystals, 6−78 ns, in which the samples were prepared using traditional chemical approaches.[36−41] Finally, the slower decay in the time-resolved PL signal confirms that the increased steady-state PL intensity of the biomineralized CdS/ZnS nanocrystals was caused by a greater tendency for photogenerated charge carriers to recombine radiatively, which is thought to occur due to passivation of surface traps by Zn.

Table 1. Parameters Obtained by Fitting a Biexponential Decay Function to the Experimental PL Decay Curves Measured for CdS and CdS/ZnS with Varying Concentrations of Zinc Acetate Added Post Synthesis[a]

amount of zinc acetate added to the sample	τ_1 (ns)	τ_2 (ns)	τ_{avg} (ns)	a_1	a_2	χ^2
0 mM	1.4	14.0	8.7	9.3×10^{-2}	1.3×10^{-2}	1.09
0.25 mM	1.6	16.7	11.7	8.7×10^{-2}	1.7×10^{-2}	1.14
0.5 mM	1.9	20.5	15.7	7.5×10^{-2}	2.0×10^{-2}	1.01
1 mM	2.0	22.6	18.2	7.1×10^{-2}	2.3×10^{-2}	0.98

[a]The far-right column contains the χ^2 goodness of fit parameter for the fitted biexponential decay functions for each sample. The χ^2 values indicate that the biexponential models fit the data well (≈1).

The peak PL intensity of CdS samples before and after zinc acetate addition was measured as a function of time to monitor how long it takes for the surface passivation process to approach equilibrium (Figure 2a). Figure 2a demonstrates that CdS by itself has a stable PL intensity, with the rapid rise at very short times due simply to the dead time between adding the zinc precursor to the CdS and beginning the measurement. The PL intensity dramatically and rapidly increases upon 1 mM zinc addition (Figure 2a), followed by a nearly constant rise until apparent equilibration after ∼15 min. Time series data presented in Figure S2 show that the PL intensity of the Cd/ZnS sample is fully equilibrated 30 min after 1 mM zinc acetate addition. These data suggest that passivation of the CdS surface by Zn^{2+} incorporation under the aqueous, ambient temperature conditions studied here occurs over two characteristic time scales. Literature studies in which CdS was passivated by ZnS under hydrothermal and solvothermal conditions between 100 and 230 °C have reported similar transient effects, with the approach to equilibrium taking between 10 min and 24 h.[8,9,11−13,31,32,36,42,43] Thus, we attribute the relatively short 15−30 min approach to equilibrium—observed here for ambient temperature con-

https://doi.org/10.1021/acsanm.1c03997
ACS Appl. Nano Mater. 2022, 5, 2293−2304

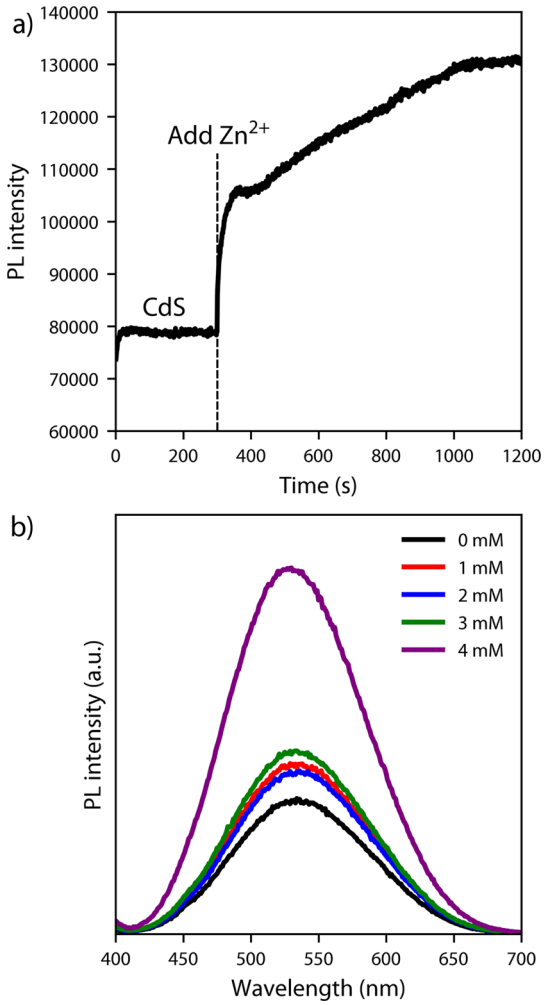

Figure 2. (a) Time-dependent steady-state fluorescence peak intensity (530 nm) of CdS nanocrystals, before and after addition of 1 mM zinc acetate to the synthesis solution at 300 s. (b) Steady-state fluorescence spectra of CdS nanocrystals after addition of increasing concentrations of zinc acetate to the synthesis solution and washing away residual components.

ditions—to the enzymatic driving force in the biomineralization solution.

While spectroscopic results suggest Zn^{2+} is incorporating on the CdS surface, it was undetermined whether Zn^{2+} was incorporating by reacting with residual HS^- in the post-biomineralization solution to form ZnS, which then attaches to the CdS surface, or if it was incorporating directly onto CdS by cation exchange or surface adsorption. Because zinc acetate was added to the synthesis solution directly after biomineralization of the CdS cores, enzymatic turnover of L-cysteine continuously generates HS^-, which could potentially react with Zn^{2+} ions in solution and thereby impact ZnS shell growth.[44] To study the impact of HS^- on the ZnS shell growth, CdS samples were washed with ethanol to remove residual HS^- and CSE and were resuspended in buffer before the addition of various concentrations of zinc acetate. Steady-state PL spectra measured for these samples (Figure 2b) reveal that residual HS^- is not necessary for the PL intensity of the samples to increase upon addition of zinc acetate. Without an obvious direct path for conversion of Zn^{2+} to ZnS in the absence of HS^-, we hypothesize that surface passivation of CdS occurs either through cation exchange or a surface adsorption process.

Confirmation of Zn^{2+} Incorporation onto CdS and Critical L-Cysteine/Metal Precursor Interdependencies. Unraveling the mechanism of Zn^{2+}-based surface passivation of CdS in the ambient temperature, aqueous biomineralization system, however, first requires the elucidation of the roles and potential interdependencies of Zn^{2+}, CdS, and L-cysteine. One limit of the room temperature ZnS shell growth process is that the addition of high concentrations of zinc acetate to the biomineralized CdS triggers aggregation of the CdS nanocrystals. While the peak PL intensity increases with addition of 4 mM zinc acetate, sols with 4 mM or greater zinc acetate destabilize after an ~1 min bench dwell time, with agglomerated particles precipitating out of solution (Figure S3a). The cause of this aggregation was likely due to competitive chelation of Zn^{2+} and Cd^{2+} by L-cysteine. Specifically, the chelation strength of L-cysteine to Cd^{2+} and Zn^{2+} species is known to be similar.[45] While L-cysteine is a reactant, it also acts as the capping ligand for the CdS/ZnS particles. Thus, addition of zinc cations to the solution likely strips L-cysteine from the surface of the CdS/ZnS particles such that the addition of high enough concentrations of Zn^{2+} removes sufficient L-cysteine to destabilize the nanoparticle sols.[28] This barrier was overcome by the addition of up to 50 mM L-cysteine into the CdS/ZnS sols, enabling stable sols with zinc acetate concentrations exceeding 20 mM, as shown in Figure S3b and further enhancement of the CdS/ZnS PL intensities (Figure S4). Additionally, Figure S4 demonstrates that having more L-cysteine in solution decreases the rate of increase in the PL intensity with increasing Zn^{2+} concentration added to the CdS sol due to L-cysteine stabilizing Zn^{2+} in solution through chelation. This relationship between PL intensity and L-cysteine also explains the results shown in Figure 2b, where the increase in the PL intensity of the CdS sols was slowed once resuspended in 8 mM L-cysteine. It should be noted that the UV−vis and PL spectra of solutions of L-cysteine and zinc acetate without biomineralized CdS (Figure S5) do not show any optical activity in the region of interest and that, as with the lower Zn^{2+} concentrations, optical spectra show no evidence of the formation of a separate ZnS nanoparticle population (Figure S6).

High-angle annular dark-field-scanning transmission electron microscopy (HAADF-STEM) images (Figure 3a−d) confirm the nanocrystalline morphology of the biomineralized CdS and CdS/ZnS particles. Both zincblende and wurtzite polymorphs of CdS were observed in the samples with 0 and 1 mM additions. The size of the CdS nanocrystals before and after surface passivation was measured to determine if incorporation of Zn^{2+} led to particle growth; comparison of the particle size distribution (PSD) data of the 0 mM and 1 mM zinc acetate samples in Figure 4a,b reveals a slight increase in particle size, although this increase was smaller than the measurement resolution. However, STEM energy-dispersive X-ray spectroscopy (XEDS) did confirm that Zn^{2+} was directly incorporating onto the CdS surface, where the 1 mM zinc acetate sample revealed the presence of a Zn-K_α signal (Figure 4d).

Zinc incorporation on the CdS nanocrystals was quantitatively measured by inductively coupled plasma optical emission spectroscopy (ICP-OES), which measured the zinc-to-cadmium ratio in the 1 mM zinc acetate sample to be 1:3.9, and furthermore, the extent of zinc incorporation on CdS increased with the concentration of zinc acetate added during the surface passivation step (Figure S8). The height of the Zn-K_α signal relative to the Cd-K_α indicates that Zn^{2+} is

https://doi.org/10.1021/acsanm.1c03997
ACS Appl. Nano Mater. 2022, 5, 2293−2304

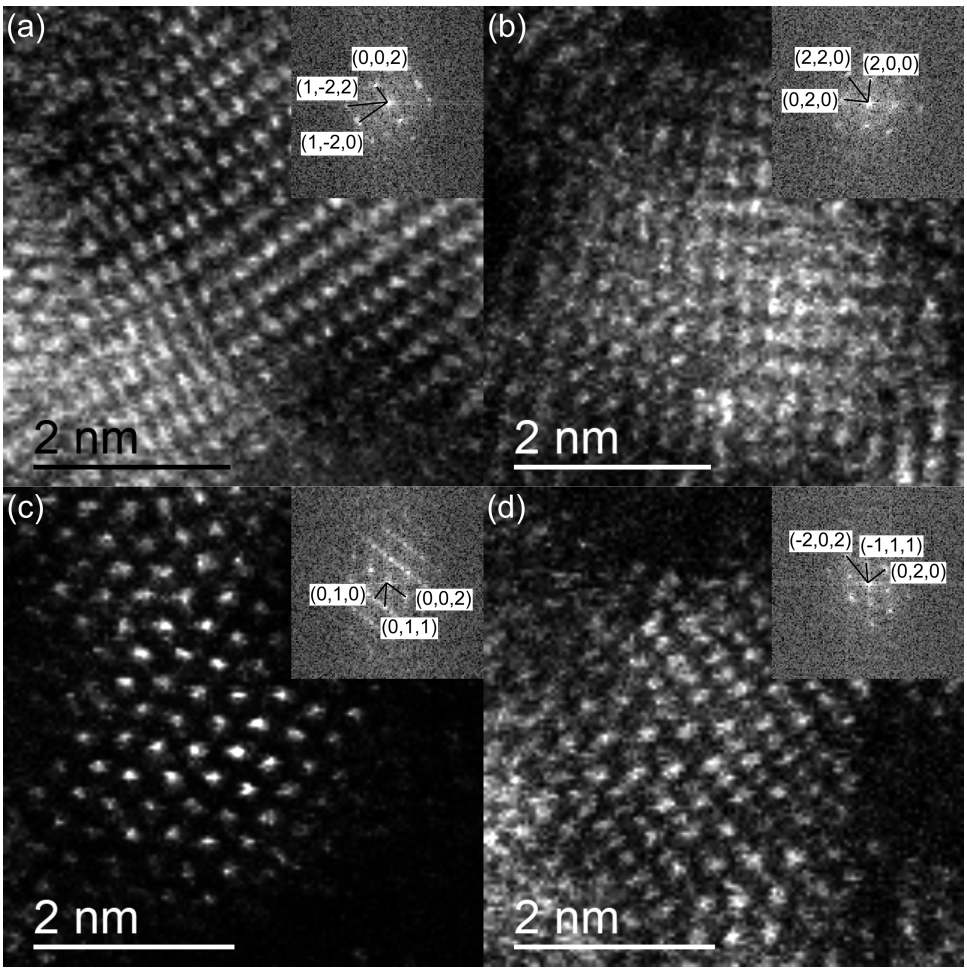

Figure 3. Representative HAADF-STEM images of crystalline CdS particles synthesized without zinc acetate addition showing the presence of (a) wurtzite polymorph oriented along the [210] zone axis and (b) zincblende polymorph oriented at the [001] zone axis. Analysis of the interplanar spacings and angles present in these images and crystallographic matching to theoretical structures is shown in Table S1. Representative HAADF-STEM images of crystalline CdS particles synthesized with 1 mM zinc acetate addition showing the presence of (c) wurtzite polymorph oriented along the [100] zone axis and (d) zincblende polymorph oriented at the [101] zone axis. Analysis of the interplanar spacings and angles present in these images and crystallographic matching to theoretical structures is shown in Table S2.

incorporated onto CdS particles with an approximate 1:4 atomic ratio of zinc-to-cadmium based on DTSA-II simulations and corroborates with ICP-OES measurements (Figure 4d).[46] Assuming full addition of zinc to the surface of CdS, we would expect an increase in particle size of less than 0.2 nm, which agrees with the measured mean particle sizes of the 0 and 1 mM samples of 1.80 and 2.23 nm, respectively (Figure 4a,b). This result, taken in conjunction with the fact the absorption and PL peak wavelengths of CdS remain the same after 0−1 mM zinc acetate addition (Figure 1b), suggests that a thin, incomplete layer of zinc forms on the surface of CdS, which would not significantly shift the peak absorbance in the PL spectra of CdS. ICP-OES and STEM-XEDS were used to confirm incorporation of Zn^{2+} onto CdS because the low extent of coverage from the ZnS layer was expected to make crystallographic observation challenging or make it difficult to determine the spatial distribution of Zn^{2+} using other techniques, like X-ray diffraction and X-ray photoelectron spectroscopy.

Wark et al. have shown that during cation exchange with cadmium chalcogenide starting materials, the solvation energies of the involved metal ions control the core−shell product thermodynamics.[47] In particular, the thermodynamic driving force of cations to be incorporated into the crystal lattice is partly dependent on the stability of the solvated ions in solution; the more stable the ions are in solution relative to the crystal lattice, the less likely they are to be incorporated into the crystal lattice. Dissolved Zn^{2+} ions solvated by water molecules are reported to have a standard Gibbs free energy of −2000 kJ mol^{-1}.[48] L-Cysteine has been demonstrated to chelate Zn^{2+} species dissolved in water, further stabilizing the molecules by approximately −25 kJ mol^{-1}.[49] By increasing the concentration of L-cysteine present during the Zn^{2+} incorporation process, the stability of the Zn^{2+} ions in solution also increases. Thus, increasing L-cysteine concentration decreases the incorporation of Zn^{2+} into the biomineralized CdS at the same zinc acetate concentrations and raises the threshold for the concentration of zinc acetate needed to see an increase in the peak PL intensity (Figure S4). Plotting the normalized PL of surface-passivated CdS against the ratio of the zinc acetate and L-cysteine concentrations used during the surface passivation process collapses the individual trends for each L-cysteine concentration observed in Figure S4 onto a single master curve (Figure S9a), further demonstrating the importance of the interaction between Zn^{2+} and L-cysteine during surface passivation.

https://doi.org/10.1021/acsanm.1c03997
ACS Appl. Nano Mater. 2022, 5, 2293−2304

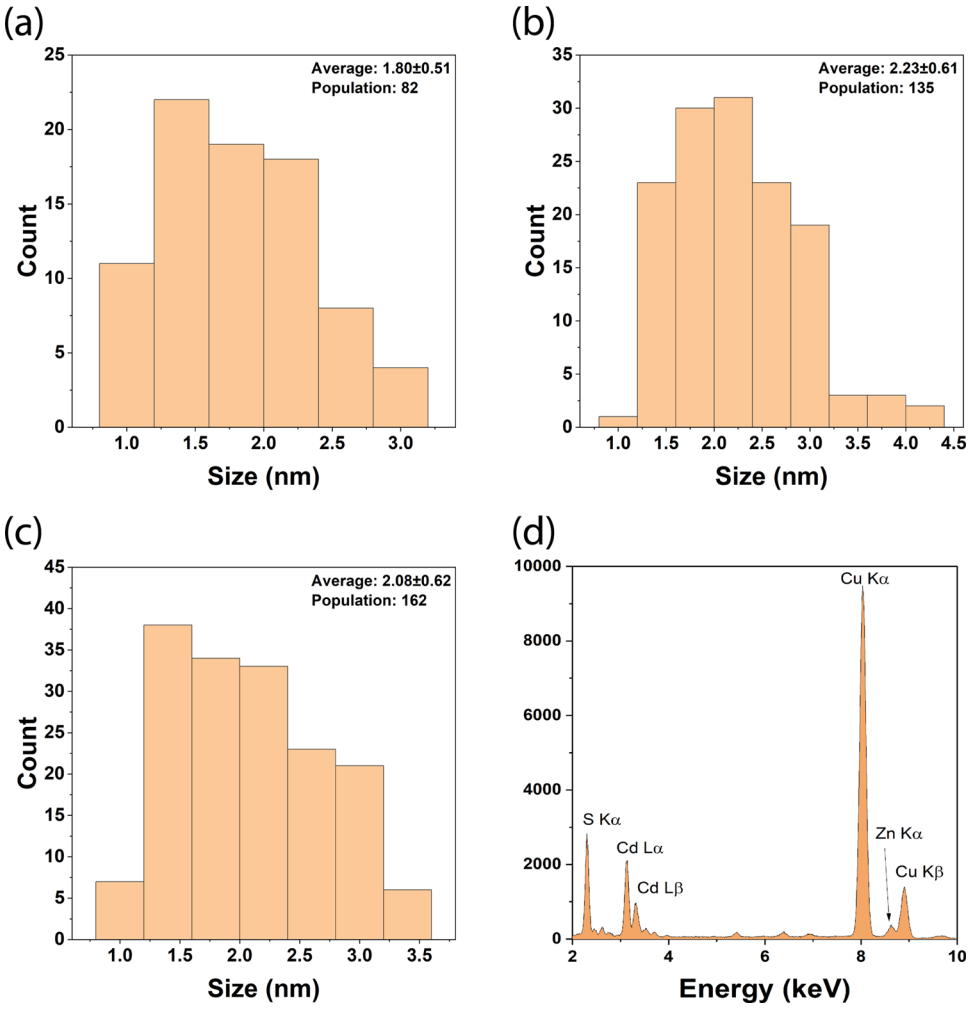

Figure 4. PSD data of CdS samples with (a) 0 mM, (b) 1 mM, and (c) 20 mM of zinc acetate used in their surface passivation step. Corresponding HAADF-STEM images of the samples in figures a–c are shown in Figure S7a–c. (d) STEM-XEDS spectrum of CdS passivated with 1 mM zinc acetate showing the coexistence of zinc and cadmium measured to have an approximate atomic ratio of 1:4 zinc-to-cadmium based on DTSA-II simulations.[47]

We hypothesize that the solvated Zn^{2+} moieties not chelated by L-cysteine are more likely than the chelated forms to passivate the surface of CdS. Indeed, the normalized PL intensities were found to positively correlate with the amount of free Zn^{2+} (see Figure S9b), estimated from L-cysteine/Zn^{2+} equilibrium data. By increasing L-cysteine concentration during the surface passivation process, we increase the free Zn^{2+} capacity of the system solution, which in turn allows for higher PL to be achieved without destabilizing particles. The surface passivation model was supported by STEM results, which found that there was not a significant change in the size distribution of particles with shells grown in 1 and 20 mM zinc precursors (Figure 4a–c). This is to be expected at room temperature because insufficient energy is supplied to overcome factors relating to shell formation, such as lattice mismatch.

Evaluating Potential Mechanisms of Zn^{2+} Incorporation. Having confirmed that Zn^{2+} is incorporating onto the CdS surface through elemental analysis and spectroscopic measurements, the mechanism of Zn^{2+} was further studied. As noted previously, incorporation of Zn^{2+} into the CdS particles was hypothesized to occur by either cation exchange or a surface adsorption process. This was because surface passivation caused by introducing Zn^{2+} to CdS nanocrystals, as observed through PL enhancement, proceeded without the presence of a reactive sulfur source, which precludes a ZnS shell growth mechanism (Figure 2b). The cation exchange process starts at the outside of the particle and proceeds inward, replacing core cations with substitute cations until a shell comprising the substitute ions is effectively formed.[47,50] In the hypothesized cation exchange mechanism, Cd^{2+} ions in the CdS lattice are replaced by Zn^{2+}. Zinc sulfide shell formation through cation exchange on metal sulfide crystals has been shown to result in a blue shift in both the PL and absorbance spectra, resulting either from alloying with the large band gap ZnS region or the shrinking of the core material.[10,34] While we observed a slight blue shift of 10 nm in the peak PL wavelength of CdS/ZnS nanocrystals synthesized from the highest concentrations of Zn^{2+} studied herein (Figure S10a), an accompanying blue shift in the UV–vis absorbance spectra was not observed (Figure S10b). Moreover, no significant change in the peak position of the optical spectra was observed for lower Zn^{2+} concentrations. Additionally, whereas the exchange of Cd^{2+} for Zn^{2+} in the CdS structure would be expected to marginally decrease the particle size due to the smaller lattice parameters of ZnS relative to CdS (Table

https://doi.org/10.1021/acsanm.1c03997
ACS Appl. Nano Mater. 2022, 5, 2293–2304

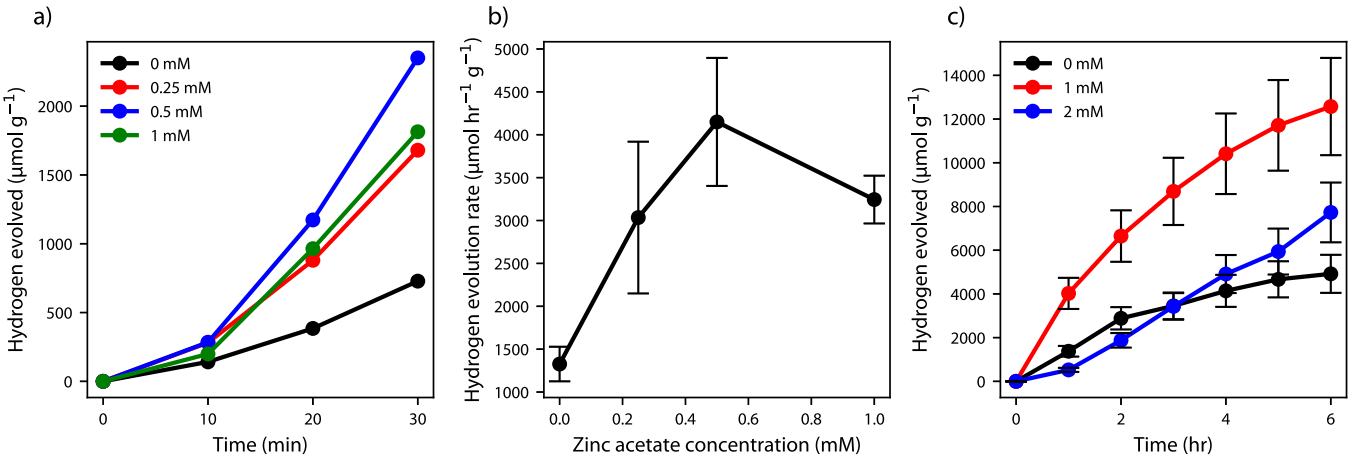

Figure 5. (a) Photocatalytic hydrogen production of biomineralized CdS with 0, 0.25, 0.5, and 1 mM of zinc acetate added during the surface passivation step and (b) respective photocatalytic hydrogen production rates of the samples obtained by linear fit of the data in part (a); (c) 6 h visible light photocatalytic hydrogen production time series of biomineralized CdS nanocrystals as a function of zinc acetate concentrations added after initial CdS nanoparticle synthesis. The particles were washed with ethanol and resuspended in Tris pH 9 with 8 mM L-cysteine to remove residual components before testing photocatalytic activity. The size of the error bars was taken to be the standard deviation of the three replicate samples.

S3),[47,51] particle size distributions collected from HAADF-STEM images before and after surface passivation show a slight increase in the particle size, albeit within the experimental uncertainty of the size distribution measurements (Figure 4a–c).

Alternatively, a second possible mechanism for CdS surface passivation is one involving facile adsorption of Zn^{2+} at either surface cation vacancies or undercoordinated surface sulfur sites, which serve as trap states for photoexcited charge carriers.[52,53] The concomitant adsorption of, at most, a monolayer of Zn^{2+} on the CdS surface would increase the particle size by roughly 0.2 nm, estimated based on ionic radii. However, the standard error of the STEM size measurements exceeds the resolution needed to discern the growth of a monolayer. While STEM-XEDS does confirm that Zn^{2+} is present in the passivated nanocrystals, the particles are too small to perform a high-resolution line-scan to determine the Zn–Cd spatial distribution. Yet, Zn^{2+} incorporation is likely taking place primarily at the particle surface since a strong blue shift in the optical spectra, which was not observed here, would be expected for whole-particle alloying.[10] The extent of Zn^{2+} incorporation is anyway expected to be low based on the measured zinc-to-cadmium ratio of 1:3.9 (Figure S8) coupled with the relatively small Zn-K_α signal and changes in STEM images of the samples when incorporating Zn^{2+} (Figure 4d). Such a low extent of exchange of Cd^{2+} for Zn^{2+} in the CdS lattice is expected based on previous studies that have established the need for high temperatures (≥100 °C) and longer times for exchange of Cd^{2+} for Zn^{2+}.[32]

Tailoring H_2 Photocatalytic Activity of Biomineralized CdS Nanoparticles by Zn^{2+} Incorporation. In general, core/shell photocatalysts can have higher activity or stability relative to the core material.[54−56] Prior investigations of photocatalytic hydrogen evolution using CdS/ZnS core/shell materials have demonstrated improvements in the photocatalytic activity and stability by decreasing charge recombination and protecting the surface from photocorrosion, respectively.[8,9] Here, we have assessed how the photocatalytic hydrogen activity of the CdS/ZnS nanocrystals, prepared under ambient, all-aqueous conditions, varies with zinc acetate concentration used for Zn^{2+} incorporation (Figure 5a,b). For these experiments, three freshly biomineralized CdS/ZnS samples were tested at each condition. All photocatalytic experiments were performed in the 100 mM Na_2S/Na_2SO_3 sacrificial reagent. Figure 5a displays the hydrogen evolution upon irradiating the photocatalysts with visible light. Passivating the surface of CdS using relatively low concentrations of zinc, between 0.25 and 1 mM, appears to more than triple the hydrogen production rate of the synthesized photocatalysts (Figure 5b). Statistical analysis (see significance testing in the Supporting Information) suggests that this increase in photocatalytic hydrogen evolution activity with increasing Zn^{2+} surface passivation is significant.

The over twofold increase in the hydrogen production rate from the 0 mM zinc acetate samples to the 0.5 mM (P = 0.02) and 1 mM (P = 0.01) zinc acetate samples (Table 2) was accompanied by low P-values (Table S4), which cast doubt on the null hypothesis that zinc acetate addition has no effect on the hydrogen evolution rate. We attribute this increase in the photocatalytic hydrogen evolution activity to the longer charge carrier lifetimes accompanying zinc acetate addition, as observed in Figure 1c. The hydrogen evolution rates of the 0.5 mM (4200 μmol h^{-1} g^{-1}) and 1 mM (3200 μmol h^{-1} g^{-1}) zinc acetate samples are consistent with the reported values, 250–10,000 h^{-1} g^{-1}, for CdS/ZnS systems synthesized by traditional high temperature, solvent-based approaches (Table S5).[8−12] The apparent decrease in the hydrogen evolution rate upon increasing the zinc acetate concentration from 0.5 to 1

Table 2. Hydrogen Evolution Rates from Biomineralized CdS Samples Passivated with 0–1 mM Zinc Acetate Added after Synthesis[a]

zinc acetate concentration (mM)	H_2 evolution rate (μmol h^{-1} g^{-1})
0 mM	1300 ± 200
0.25 mM	3000 ± 900
0.5 mM	4200 ± 800
1 mM	3200 ± 300

[a]Significance testing data from these results are given in Table S4.

https://doi.org/10.1021/acsanm.1c03997
ACS Appl. Nano Mater. 2022, 5, 2293−2304

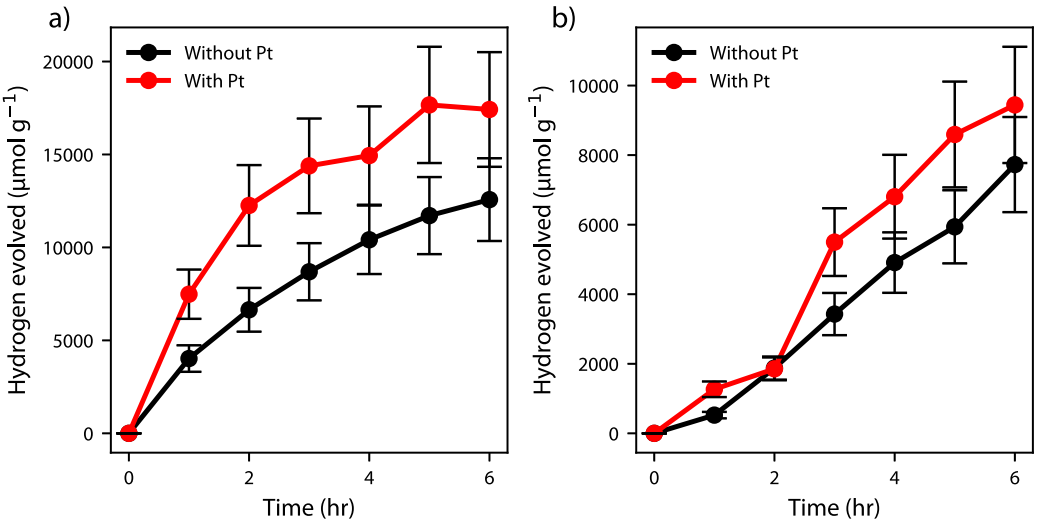

Figure 6. Six hour visible light photocatalytic hydrogen production time series of biomineralized CdS nanocrystals with (a) 1 mM and (b) 2 mM zinc acetate used during the surface passivation step with and without a photodeposited platinum cocatalyst. The loading of the platinum cocatalyst used during this step was 10 wt %. The particles were washed with ethanol and resuspended in Tris pH 9 with 8 mM L-cysteine to remove residual components before testing photocatalytic activity.

mM was possibly due to overpassivation of the CdS surface with Zn^{2+}.

In fact, further increasing the concentration of zinc acetate in the shell growth step beyond 1 mM was found to dramatically affect the hydrogen production (Figure S11), with zinc acetate concentrations of 4 mM or greater effectively deactivating the resulting photocatalysts. A similar phenomenon was reported by Abdellah et al. and Sun et al. when investigating charge transfer from a metal chalcogenide core through a wide band gap ZnS shell to a metal oxide electron acceptor. They found that growth of the insulating ZnS shell increased the PL quantum yield by passivating surface traps while simultaneously decreasing the electron transfer rate from the metal sulfide core to the metal oxide electron acceptor due to the increased distance between the photoexcited electrons on the metal sulfide and the electron acceptor.[26,27] In the study by Abdellah et al., growing a ZnS shell greater than ∼1 monolayer in thickness on a CdSe core was found to negatively affect the electron injection efficiency into a ZnO electron acceptor.[26] Additionally, other studies have shown a decrease in the photocatalytic H_2 evolution rate of $Cd_xZn_{1-x}S$ alloys caused by widening of the band gap, which reduces the efficiency of photon absorption.[10]

Band gap widening is not suspected in the present study given negligible blue shifts in the UV−vis absorption and PL spectra of the biomineralized CdS after Zn^{2+} incorporation (see Figures 1b and S10). The observed deactivation at the highest concentrations of zinc acetate is instead more likely due to covering of the active CdS surface at the higher concentrations of zinc acetate, thus limiting access and mitigating charge transfer to surface-bound reactant species. Previous experimental studies of type-I CdS/ZnS core−shell photocatalysts have attempted to overcome the charge transfer barrier presented by a thick insulative shell by introducing mesoporosity in the shell to allow for surface accessibility of reactant species.[9] As previously discussed in the case of modest concentrations of zinc acetate used for shell growth (i.e., up to 1 mM), Zn^{2+} appears to only partially cover the surface of the biomineralized CdS materials studied herein as a result of thermodynamic and kinetic limitations at room temperature and lattice mismatch between the two phases. As in the case of the mesoporous ZnS shells, tuning zinc acetate concentrations in the all-aqueous, ambient temperature system studied herein appears to ensure sufficient sub-monolayer Zn^{2+} coverage of the CdS particles to enable a high photoexcited electron lifetime while allowing for electrons to react with surface-bound species.[9]

Stability-Activity Trade-Off of Zn^{2+}-Passivated CdS. CdS photocatalysts are generally unstable due to the photooxidation and dissolution of the catalyst. Photogenerated holes produced by CdS have the potential to oxidize cadmium lattice sites causing dissolution of the catalyst over time, as depicted in the following reaction.[57]

$$CdS + 2h^+ \rightarrow Cd^{2+} + S \quad (2)$$

Adding a ZnS shell on CdS has been demonstrated to improve photocatalytic stability by protecting these surface sites from oxidation.[8,9] Extended-time photocatalytic studies were performed to understand how the incorporation of Zn^{2+} onto CdS affected catalyst stability. We find that the stability of the CdS/ZnS photocatalyst developed herein is dependent on the zinc acetate concentration used for Zn^{2+}-based passivation (Figure 5c). While there is a significant increase in hydrogen production upon introduction of Zn^{2+} at a concentration of 1 mM, the stability of the resulting photocatalyst is practically the same as the native CdS particles. We attribute the decay in the hydrogen evolution rates occurring after about 2 h for both the native and Zn^{2+}-passivated CdS to photocorrosion. Increasing the Zn^{2+} concentration to 2 mM results in a more stable but less active photocatalyst that retains its hydrogen evolution activity through the 6 h testing period, but only at a decreased activity equivalent to that of the native CdS. Time-resolved PL studies of the 0, 1, and 2 mM Zn^{2+} samples show an increase in the PL lifetime of the samples with increased zinc acetate concentration, which indicates increased surface passivation (Figure S12). Thus, the decrease in the hydrogen evolution rate for the 2 mM Zn^{2+} sample is attributed to reduced charge transport properties resulting from the overpassivation of the core CdS surface.[26] After 8 h, the 2 mM zinc acetate sample is inactive (Figure S13). Clearly,

https://doi.org/10.1021/acsanm.1c03997
ACS Appl. Nano Mater. 2022, 5, 2293−2304

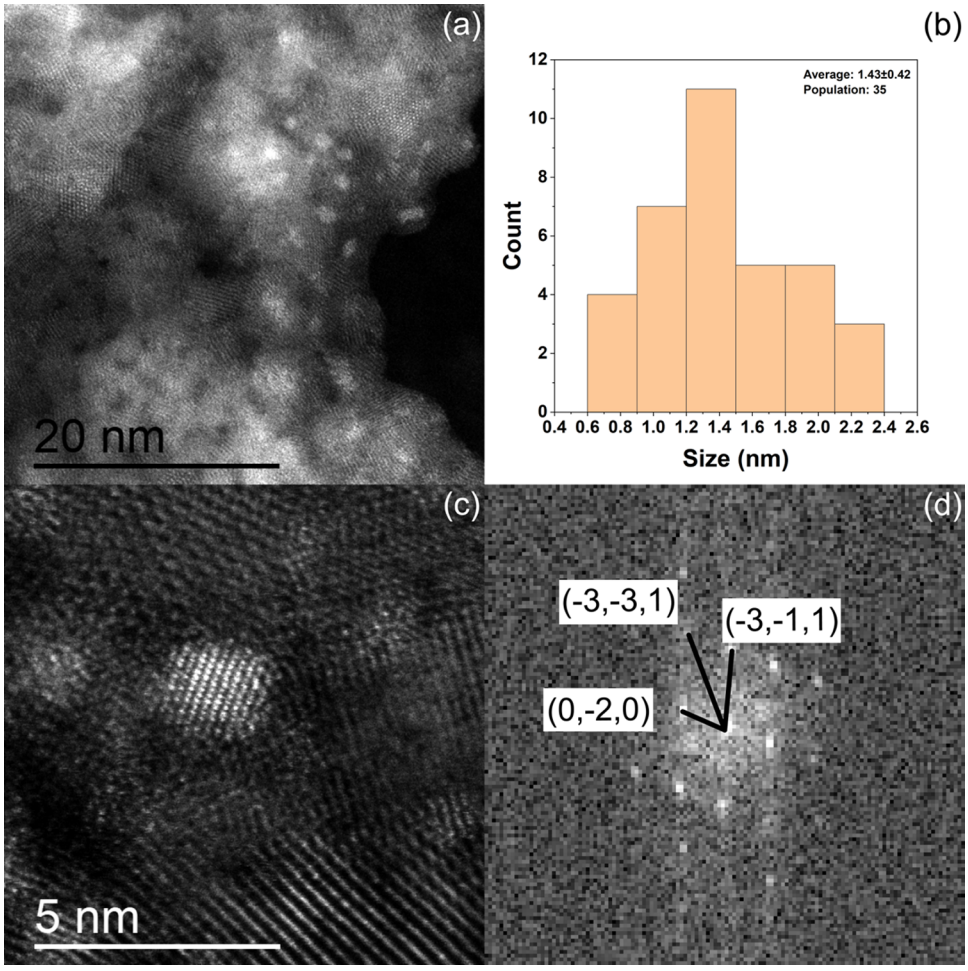

Figure 7. STEM analysis of the CdS/ZnS photocatalyst with 10% platinum cocatalyst addition showing (a) HAADF-STEM image of the intimate distribution of the platinum cocatalyst (brighter particles) within the darker CdS/ZnS support; (b) PSD analysis of the platinum cocatalyst; (c) atomic resolution HAADF-STEM image of a typical platinum particle; and (d) corresponding indexed FFT of the particle shown in figure c, which matched well to the [103] zone axis for fcc platinum.

precise control of the Zn^{2+} surface coverage on CdS is necessary to navigate the trade-off between enhancing the photocatalytic activity and maximizing catalyst stability.

Enhancing H_2 Photocatalytic Activity with Platinum Cocatalyst Incorporation. Incorporation of platinum cocatalysts onto CdS/ZnS nanoparticles has been demonstrated to enhance their photocatalytic hydrogen evolution rates.[8,10] The photocatalytic hydrogen evolution from biomineralized CdS passivated with 1 and 2 mM Zn^{2+} and in the presence or absence of 10 wt % photodeposited platinum is shown in Figure 6a,b. In both cases, the addition of the platinum cocatalyst increases the hydrogen evolution activity relative to the cocatalyst-free sample. In the presence of the platinum cocatalyst, the initial hydrogen evolution rates from the 1 and 2 mM Zn^{2+} samples were 7500 and 1200 μmol h^{-1} g^{-1}, respectively, which are comparable with reported rates for CdS/ZnS photocatalysts synthesized through high temperature means with platinum cocatalyts.[8,10] After 6 h of continuous testing, the total hydrogen production by the 1 mM zinc acetate CdS sample with the platinum cocatalyst exceeded by 40% compared to the corresponding platinum-free photocatalyst. Similarly, photodeposition of a platinum cocatalyst on the 2 mM zinc acetate CdS sample improved its total hydrogen production over the 6 h period by 20%. General trends in the long-term stability of the photocatalysts, however, were not altered by platinum photodeposition; the hydrogen evolution rate of the 1 mM Zn^{2+} sample, while higher initially, decayed within the first 2 h due to photocorrosion while the hydrogen evolution rate of the 2 mM Zn^{2+} sample was relatively stable throughout the entire 6 h testing period.

STEM analysis of the CdS/ZnS photocatalyst containing the additional photoreduced platinum cocatalyst confirmed the intimate mixing of the component nanoparticles as shown in Figure 7a. The small platinum particles, dispersed homogeneously over the CdS/ZnS photocatalyst, were found to have an average particle size of 1.43 nm as shown in Figure 7b. The crystallinity of a typical platinum nanoparticle is shown in Figure 7c, which was confirmed to match the [103] zone axis of fcc platinum as shown in Figure 7d and Table S6. No large agglomerations of platinum particles were observed in the sample, but Figure 7c does indicate the possibility of some atomically dispersed platinum species.

■ CONCLUSIONS

We have demonstrated that room temperature incorporation of Zn^{2+} onto biomineralized CdS passivates surface traps, increasing steady-state PL peak intensity and PL lifetime. The biomineralization synthesis approach allows us to significantly

https://doi.org/10.1021/acsanm.1c03997
ACS Appl. Nano Mater. 2022, 5, 2293−2304

decrease the synthesis temperature of the CdS/ZnS nanocrystals, to 37 °C, relative traditional synthesis pathways. The extent of the surface passivation process is controlled by the concentration of the zinc precursor added directly to the biomineralized CdS solution; the higher the concentration Zn^{2+}, the greater the extent of the surface passivation. Incorporation of Zn^{2+} onto the CdS surface was independently confirmed by ICP-OES and STEM-XEDS, which measured the zinc-to-cadmium ratio of the washed CdS/ZnS product to be 1:3.9 and 1:4, respectively. The surface passivation occurs rapidly (≤15 min) and does not require residual HS^-, indicating that either a surface adsorption or cation exchange process likely governs Zn^{2+} incorporation into the biomineralized CdS nanoparticles. Photocatalytic studies, using a Na_2S/Na_2SO_3 sacrificial reagent, revealed an increase in the photocatalytic hydrogen evolution rate of the biomineralized CdS with increasing Zn^{2+} up to 1 mM, which was attributed to the resulting increase in charge carrier lifetime. Once an optimum Zn^{2+} concentration, and thereby the optimum degree of CdS surface passivation, was achieved, photocatalytic hydrogen evolution rates decreased with additional Zn^{2+} despite increasing PL lifetimes and improving photostability. The decrease in the photocatalytic hydrogen evolution rate at high Zn^{2+} concentrations is attributed to overpassivation of the CdS surface and thus the formation of a barrier for charges to transfer to the surface for reaction. Photodeposition of a platinum cocatalyst on the Zn^{2+}-passivated CdS did not impact photostability but did further enhance the hydrogen evolution rate as expected, with the greatest improvement observed for the highest-performing CdS/ZnS photocatalyst. Ultimately, this work establishes a facile process for precisely controlling the passivation of biomineralized photocatalysts, and thereby obtaining a versatile all-aqueous phase, ambient temperature synthetic platform for functional materials with performance rivaling materials derived from much harsher, less sustainable conditions.

EXPERIMENTAL SECTION

Biomineralization of CdS Quantum Dots. L-Cysteine-capped CdS nanocrystals were biomineralized by incubating 1 mM cadmium acetate (Alfa Aesar, 99.999% Puratronic) with our engineered CSE enzyme and 8 mM L-cysteine (Spectrum Chemical, 98%) in a Tris buffered (pH 9) solution at 37 °C. As we have previously demonstrated,[20] these conditions promote the enzymatic turnover of L-cysteine by CSE to generate reactive HS^- species that can then react with Cd^{2+} in solution to form CdS nanocrystals. Size control of the nanocrystals is achieved via the relatively slow and constant background level of the generated HS^- species, which serves to keep the nanocrystal growth mechanism within the size-focusing regime throughout the 4 h growth period.[50] The growing nanocrystals are capped by the dissociated thiol groups of unreacted L-cysteine, both stabilizing the crystals in solution and acting to further control particle growth. The biomineralized CdS nanocrystals used for the experiment had a UV−vis absorption peak at 390 nm with an absorption of 1.4, which corresponded to a particle concentration of 5 μM.[29]

Surface Passivation of Biomineralized CdS with Zn^{2+}. Following biomineralization and before any cleaning steps, an aliquot of zinc acetate (Sigma-Aldrich, 99.995%) was added to the as-synthesized CdS. The sample was placed on an orbital shaker for 15 min following the addition of the zinc precursor before further characterization. When passivating biomineralized CdS with zinc acetate concentrations of ≥4 mM, the CdS solution was replenished with L-cysteine before adding zinc acetate to keep particles stable. The nanocrystals were precipitated by mixing the sol with ethanol, centrifuging, and resuspending in Tris pH 9 with 8 mM L-cysteine to remove any residual components.

Photocatalytic H_2 Generation. Photocatalyst samples were tested for H_2 generation by suspending the material in 80 mL of 0.1 M Na_2S/0.1 M Na_2SO_3. The sacrificial reagent was necessary to accept photogenerated holes as the synthesized CdS photocatalysts could not evolve oxygen from water due to slow kinetics. The sacrificial reagent was chosen because Na_2S provides S^{2-} anions which can be oxidized by photogenerated holes and Na_2SO_3 suppresses the formation of disulfide species that can reduce hydrogen evolution efficiency.[58] Before testing, glassware was rinsed with concentrated sulfuric acid to remove noble metal impurities that can uncontrollably affect photocatalytic performance. The suspension was degassed under vacuum for 15 min in a 100 mL round-bottom flask while stirring. The remaining head space was then purged with N_2. A 0.4 mL of gas sample was taken from the purged reactor to ensure that there was negligible oxygen in the flask. The reactor was then sealed and positioned 20 cm away from a 350 W xenon lamp fitted with a 420 nm long-pass cutoff filter (Newport), which provided an illumination intensity of approximately 1000 W m^{-2}. A 0.4 mL of gas sample was obtained every 30 min through a septum and analyzed for hydrogen content. All gas content analyses were done using a model 8610C gas chromatograph (SRI Instruments) equipped with a thermal conductivity detector. For samples with a platinum cocatalyst, the platinum component was photodeposited by adding 13 μM of chloroplatinic acid hexahydrate (Sigma-Aldrich, 99.995%) to the CdS photocatalyst in a sacrificial reagent, equaling a 10 wt % loading of Pt. The mixture was then irradiated for 30 min using an unfiltered 350 W xenon lamp situated 20 cm away from the sample, followed by purging the system with N_2 before any further testing. A 2 mg mass of the catalyst was used for each run.

Material Characterization. Absorbance measurements were collected using a Shimadzu UV−vis 2600 spectrophotometer equipped with an ISR-2600-Plus integrating sphere attachment. PL spectra were acquired using a QuantaMaster 400 instrument (Photon Technology International). PL lifetime measurements were obtained using a Fluorolog-3 spectrofluorometer with an attached TCSPC controller using a 287 nm laser (Delta Diode) excitation source, and measurements were taken at 530 nm. Samples were structurally characterized using an aberration-corrected JEM-ARM200CF transmission electron microscope equipped with a HAADF detector and a centurion XEDS spectrometer. The microscope was operated at 80 kV in STEM mode to characterize nanoparticle size, composition, and crystallography, as well as the spatial distribution of CdS and platinum in our photocatalysts. ICP-OES analysis was performed on a PerkinElmer ICP-OES Optima 2100DV; ICP-OES samples were prepared by washing CdS nanocrystals post surface passivation and dissolved in ∼1 M HNO_3.

ASSOCIATED CONTENT

Supporting Information

The Supporting Information is available free of charge at https://pubs.acs.org/doi/10.1021/acsanm.1c03997.

Additional spectroscopic, elemental, and STEM characterization as well as supplementary catalytic data (PDF)

AUTHOR INFORMATION

Corresponding Author

Steven McIntosh − *Department of Chemical and Biomolecular Engineering, Lehigh University, Bethlehem, Pennsylvania 18015, United States;* orcid.org/0000-0003-4664-2028; Email: mcintosh@lehigh.edu

Authors

John Sakizadeh − *Department of Chemical and Biomolecular Engineering, Lehigh University, Bethlehem, Pennsylvania 18015, United States*

https://doi.org/10.1021/acsanm.1c03997
ACS Appl. Nano Mater. 2022, 5, 2293−2304

Joseph P. Cline − *Department of Materials Science and Engineering, Lehigh University, Bethlehem, Pennsylvania 18015, United States*

Mark A. Snyder − *Department of Chemical and Biomolecular Engineering, Lehigh University, Bethlehem, Pennsylvania 18015, United States;* orcid.org/0000-0002-8925-0588

Christopher J. Kiely − *Department of Chemical and Biomolecular Engineering and Department of Materials Science and Engineering, Lehigh University, Bethlehem, Pennsylvania 18015, United States*

Complete contact information is available at: https://pubs.acs.org/10.1021/acsanm.1c03997

Notes

The authors declare no competing financial interest.

■ ACKNOWLEDGMENTS

We acknowledge support from the National Science Foundation under the SNM program, Grant No. 1727166. We thank Prof. Angela Brown of the Department of Chemical Engineering at Lehigh University for allowing us use of her fluorometer. We also thank Prof. Arup SenGupta of the Department of Civil & Environmental Engineering for use of the ICP-OES and graduate student, Hao Chen, also of the Department of Civil & Environmental Engineering for assistance in performing the measurements.

■ REFERENCES

(1) Wang, Q.; Domen, K. Particulate Photocatalysts for Light-Driven Water Splitting: Mechanisms, Challenges, and Design Strategies. *Chem. Rev.* **2019**, *120*, 919−985.

(2) Dunleavy, R.; Lu, L.; Kiely, C. J.; McIntosh, S.; Berger, B. W. Single-Enzyme Biomineralization of Cadmium Sulfide Nanocrystals with Controlled Optical Properties. *Proc. Natl. Acad. Sci. U. S. A.* **2016**, *113*, 5275−5280.

(3) Kang, S. H.; Bozhilov, K. N.; Myung, N. V.; Mulchandani, A.; Chen, W. Microbial Synthesis of CdS Nanocrystals in Genetically Engineered *E. Coli*. *Angew. Chem., Int. Ed.* **2008**, *120*, 5264−5267.

(4) Li, Q.; Li, X.; Wageh, S.; Al-Ghamdi, A. A.; Yu, J. CdS/Graphene Nanocomposite Photocatalysts. *Adv. Energy Mater.* **2015**, *5*, No. 1500010.

(5) Yin, X.; Li, L.; Jiang, W.; Zhang, Y.; Zhang, X.; Wan, L.; Hu, J. MoS_2/CdS Nanosheets-on-Nanorod Heterostructure for Highly Efficient Photocatalytic H_2 Generation Under Visible Light Irradiation. *ACS Appl. Mater. Interfaces* **2016**, *8*, 15258−15266.

(6) Yang, G.; Yan, W.; Zhang, Q.; Shen, S.; Ding, S. One-Dimensional CdS/ZnO Core/Shell Nanofibers via Single-Spinneret Electrospinning: Tunable Morphology and Efficient Photocatalytic Hydrogen Production. *Nanoscale* **2013**, *5*, 12432−12439.

(7) Low, J.; Yu, J.; Jaroniec, M.; Wageh, S.; Al-Ghamdi, A. A. Heterojunction Photocatalysts. *Adv. Mater.* **2017**, *29*, No. 1601694.

(8) Huang, L.; Wang, X.; Yang, J.; Liu, G.; Han, J.; Li, C. Dual Cocatalysts Loaded Type I CdS/ZnS Core/Shell Nanocrystals as Effective and Stable Photocatalysts for H_2 Evolution. *J. Phys. Chem. C* **2013**, *117*, 11584−11591.

(9) Xie, Y. P.; Yu, Z. B.; Liu, G.; Ma, X. L.; Cheng, H. CdS−Mesoporous ZnS Core−Shell Particles for Efficient and Stable Photocatalytic Hydrogen Evolution Under Visible Light. *Energy Environ. Sci.* **2014**, *7*, 1895−1901.

(10) Wang, J.; Li, B.; Chen, J.; Li, N.; Zheng, J.; Zhao, J.; Zhu, Z. Enhanced Photocatalytic H_2-Production Activity of $Cd_xZn_{1-x}S$ Nanocrystals by Surface Loading MS (M = Ni, Co, Cu) Species. *Appl. Surf. Sci.* **2012**, *259*, 118−123.

(11) Lin, Y.; Zhang, Q.; Li, Y.; Liu, Y.; Xu, K.; Huang, J.; Zhou, X.; Peng, F. The Evolution from a Typical Type-I CdS/ZnS to Type-II and Z-Scheme Hybrid Structure for Efficient and Stable Hydrogen Production Under Visible Light. *ACS Sustainable Chem. Eng.* **2020**, *8*, 4537−4546.

(12) Kundu, J.; Satpathy, B. K.; Pradhan, D. Composition-Controlled CdS/ZnS Heterostructure Nanocomposites for Efficient Visible Light Photocatalytic Hydrogen Generation. *Ind. Eng. Chem. Res.* **2019**, *58*, 22709−22717.

(13) Reddy, N. L.; Rao, V. N.; Kumari, M. M.; Sathish, M.; Venkatakrishnan, S. M. Development of High Quantum Efficiency CdS/ZnS core/shell Structured Photocatalyst for the Enhanced Solar Hydrogen Evolution. *Int. J. Hydrogen Energy* **2018**, *43*, 22315−22328.

(14) Zhou, J.; Yang, Y.; Zhang, C. Toward Biocompatible Semiconductor Quantum Dots: from Biosynthesis and Bioconjugation to Biomedical Application. *Chem. Rev.* **2015**, *115*, 11669−11717.

(15) Spangler, L. C.; Chu, R.; Lu, L.; Kiely, C. J.; Berger, B. W.; McIntosh, S. Enzymatic Biomineralization of Biocompatible $CuInS_2$, $(CuInZn)S_2$ and $CuInS_2$/ZnS Core/Shell Nanocrystals for Bioimaging. *Nanoscale* **2017**, *9*, 9340−9351.

(16) Sadeghnejad, A.; Lu, L.; Kiely, C. J.; Berger, B. W.; McIntosh, S. Single Enzyme Direct Biomineralization of ZnS, $Zn_xCd_{1-x}S$ and $Zn_xCd_{1-x}S$-ZnS Quantum Confined Nanocrystals. *RSC Adv.* **2017**, *7*, 38490−38497.

(17) Sakizadeh, J.; Cline, J. P.; Snyder, M. A.; Kiely, C. J.; McIntosh, S. Tailored Coupling of Biomineralized CdS Quantum Dots to rGO to Realize Ambient Aqueous Synthesis of a High-Performance Hydrogen Evolution Photocatalyst. *ACS Appl. Mater. Interfaces* **2020**, *12*, 42773−42780.

(18) Yang, Z.; Lu, L.; Kiely, C. J.; Berger, B. W.; McIntosh, S. Biomineralized CdS Quantum Dot Nanocrystals: Optimizing Synthesis Conditions and Improving Functional Properties by Surface Modification. *Ind. Eng. Chem. Res.* **2016**, *55*, 11235−11244.

(19) Spangler, L. C.; Cline, J. P.; Kiely, C. J.; McIntosh, S. Low Temperature Aqueous Synthesis of Size-Controlled Nanocrystals Through Size Focusing: a Quantum Dot Biomineralization Case Study. *Nanoscale* **2018**, *10*, 20785−20795.

(20) Spangler, L. C.; Cline, J. P.; Sakizadeh, J. D.; Kiely, C. J.; McIntosh, S. Enzymatic Synthesis of Supported CdS Quantum Dot/Reduced Graphene Oxide Photocatalysts. *Green Chem.* **2019**, *21*, 4046−4054.

(21) Sadeghnejad, A.; Lu, L.; Cline, J.; Ozdemir, N. K.; Snyder, M. A.; Kiely, C. J.; McIntosh, S. In Situ Biomineralization of $Cu_xZn_ySn_zS_4$ Nanocrystals within TiO_2-Based Quantum Dot Sensitized Solar Cell Anodes. *ACS Appl. Mater. Interfaces* **2019**, *11*, 45656−45664.

(22) Yang, Z.; Lu, L.; Kiely, C. J.; Berger, B. W.; McIntosh, S. Single Enzyme Direct Biomineralization of CdSe and CdSe-CdS Core-Shell Quantum Dots. *ACS Appl. Mater. Interfaces* **2017**, *9*, 13430−13439.

(23) Curran, C. D.; Lu, L.; Jia, Y.; Kiely, C. J.; Berger, B. W.; McIntosh, S. Direct Single-Enzyme Biomineralization of Catalytically Active Ceria and Ceria-Zirconia Nanocrystals. *ACS Nano* **2017**, *11*, 3337−3346.

(24) Spangler, L. C.; Lu, L.; Kiely, C. J.; Berger, B. W.; McIntosh, S. Biomineralization of PbS and PbS-CdS Core-Shell Nanocrystals and Their Application in Quantum Dot Sensitized Solar Cells. *J. Mater. Chem. A* **2016**, *4*, 6107−6115.

(25) Yang, Z.; Lu, L.; Berard, V. F.; He, Q.; Kiely, C. J.; Berger, B. W.; McIntosh, S. Biomanufacturing of CdS Quantum Dots. *Green Chem.* **2015**, *17*, 3775−3782.

(26) Abdellah, M.; Zidek, K.; Zheng, K.; Chábera, P.; Messing, M. E.; Pullerits, T. Balancing Electron Transfer and Surface Passivation in Gradient CdSe/ZnS Core−Shell Quantum Dots Attached to ZnO. *J. Phys. Chem. Lett.* **2013**, *4*, 1760−1765.

(27) Sun, J.; Zhao, J.; Masumoto, Y. Shell-Thickness-Dependent Photoinduced Electron Transfer from $CuInS_2$/ZnS Quantum Dots to TiO_2 Films. *Appl. Phys. Lett.* **2013**, *102*, No. 053119.

(28) Bae, W.; Abdullah, R.; Mehra, R. K. Cysteine-Mediated Synthesis of CdS Bionanocrystallites. *Chemosphere* **1998**, *37*, 363−385.

(29) Yu, W. W.; Qu, L.; Guo, W.; Peng, X. Experimental Determination of the Extinction Coefficient of CdTe, CdSe, and CdS Nanocrystals. *Chem. Mater.* **2003**, *15*, 2854−2860.

(30) Dabbousi, B. O.; Rodriguez-Viejo, J.; Mikulec, F. V.; Heine, J. R.; Mattoussi, H.; Ober, R.; Jensen, K. F.; Bawendi, M. G. (CdSe)ZnS core−shell Quantum Dots: Synthesis and Characterization of a Size Series of Highly Luminescent Nanocrystallites. *J. Phys. Chem. B* **1997**, *101*, 9463−9475.
(31) Steckel, J. S.; Zimmer, J. P.; Coe-Sullivan, S.; Stott, N. E.; Bulović, V.; Bawendi, M. G. Blue Luminescence from (CdS)ZnS Core−Shell Nanocrystals. *Angew. Chem., Int. Ed.* **2004**, *116*, 2206−2210.
(32) Choi, D.; Pyo, J.; Kim, Y.; Jang, D. Facile Synthesis of Composition-Gradient Cd_{1-x} Zn_xS Quantum Dots by Cation Exchange for Controlled Optical Properties. *J. Mater. Chem. C* **2015**, *3*, 3286−3293.
(33) Li, H.; Zanella, M.; Genovese, A.; Povia, M.; Falqui, A.; Giannini, C.; Manna, L. Sequential Cation Exchange in Nanocrystals: Preservation of Crystal Phase and Formation of Metastable Phases. *Nano Lett.* **2011**, *11*, 4964−4970.
(34) Park, J.; Kim, S. $CuInS_2$/ZnS Core/Shell Quantum Dots by Cation Exchange and Their Blue-Shifted Photoluminescence. *J. Mater. Chem.* **2011**, *21*, 3745−3750.
(35) Labeau, O.; Tamarat, P.; Lounis, B. Temperature Dependence of the Luminescence Lifetime of Single CdSe/ZnS Quantum Dots. *Phys. Rev. Lett.* **2003**, *90*, No. 257404.
(36) Gray, V.; Xia, P.; Huang, Z.; Moses, E.; Fast, A.; Fishman, D. A.; Vullev, V. I.; Abrahamsson, M.; Moth-Poulsen, K.; Tang, M. L. CdS/ZnS Core−Shell Nanocrystal Photosensitizers for Visible to UV Upconversion. *Chem. Sci.* **2017**, *8*, 5488−5496.
(37) Liu, X.; Jiang, Y.; Lan, X.; Zhang, Y.; Li, S.; Li, J.; Han, T.; Wang, B.; Zhong, H. Highly Luminescent Blue Emitting CdS/ZnS Core/Shell Quantum Dots via a Single-Molecular Precursor for Shell Growth. *Mater. Chem. Phys.* **2011**, *130*, 909−914.
(38) Phadnis, C.; Sonawane, K. G.; Hazarika, A.; Mahamuni, S. Strain-Induced Hierarchy of Energy Levels in CdS/ZnS Nanocrystals. *J. Phys. Chem. C* **2015**, *119*, 24165−24173.
(39) Liu, L.; Hu, S.; Pan, Y.; Zhang, J.; Feng, Y.; Zhang, X. Optimizing the Synthesis of CdS/ZnS Core/Shell Semiconductor Nanocrystals for Bioimaging Applications. *Beilstein J. Nanotechnol.* **2014**, *5*, 919−926.
(40) Jones, M.; Lo, S. S.; Scholes, G. D. Quantitative Modeling of the Role of Surface Traps in CdSe/CdS/ZnS Nanocrystal Photoluminescence Decay Dynamics. *Proc. Natl. Acad. Sci. U. S. A.* **2009**, *106*, 3011−3016.
(41) Issac, A.; Jin, S.; Lian, T. Intermittent Electron Transfer Activity from Single CdSe/ZnS Quantum Dots. *J. Am. Chem. Soc.* **2008**, *130*, 11280−11281.
(42) Liu, F.; Xiao, C.; Meng, L.; Chen, L.; Zhang, Q.; Liu, J.; Shen, S.; Guo, J.; Au, C.; Yin, S. Facile Fabrication of Octahedral CdS−ZnS by Cation Exchange for Photocatalytic Toluene Selective Oxidation. *ACS Sustainable Chem. Eng.* **2020**, *8*, 1302−1310.
(43) Aboulaich, A.; Billaud, D.; Abyan, M.; Balan, L.; Gaumet, J.; Medjadhi, G.; Ghanbaja, J.; Schneider, R. One-Pot Noninjection Route to CdS Quantum Dots via Hydrothermal Synthesis. *ACS Appl. Mater. Interfaces* **2012**, *4*, 2561−2569.
(44) Al-Tarazi, M.; Heesink, A. B. M.; Versteeg, G. F.; Azzam, M. O.; Azzam, K. Precipitation of CuS and ZnS in a Bubble Column Reactor. *AIChE J.* **2005**, *51*, 235−246.
(45) Walsh, M. J.; Ahner, B. A. Determination of Stability Constants of Cu(I), Cd(II) & Zn(II) Complexes with Thiols Using Fluorescent Probes. *J. Inorg. Biochem.* **2013**, *128*, 112−123.
(46) Ritchie, N. NIST DTSA-II. https://www.cstl.nist.gov/div837/837.02/epq/dtsa2/index.html (accessed March 20, 2018).
(47) Wark, S. E.; Hsia, C.; Son, D. H. Effects of Ion Solvation and Volume Change of Reaction on the Equilibrium and Morphology in Cation-Exchange Reaction of Nanocrystals. *J. Am. Chem. Soc.* **2008**, *130*, 9550−9555.
(48) Marcus, Y. Thermodynamics of Solvation of Ions. *J. Chem. Soc., Faraday Trans.* **1991**, *87*, 2995−2999.
(49) Yang, N.; Wang, X.; Wan, Q. Electrochemical Reduction of Zn(II) Ions on L-cysteine Coated Gold Electrodes. *Electrochim. Acta* **2006**, *51*, 2050−2056.
(50) Groeneveld, E.; Witteman, L.; Lefferts, M.; Ke, X.; Bals, S.; Van Tendeloo, G.; de Mello Donega, C. Tailoring ZnSe−CdSe Colloidal Quantum Dots *via* Cation Exchange: from Core/Shell to Alloy Nanocrystals. *ACS Nano* **2013**, *7*, 7913−7930.
(51) Talapin, D. V.; Mekis, I.; Götzinger, S.; Kornowski, A.; Benson, O.; Weller, H. CdSe/CdS/ZnS and CdSe/ZnSe/ZnS Core−Shell−Shell Nanocrystals. *J. Phys. Chem. B* **2004**, *108*, 18826−18831.
(52) Justo, Y.; Sagar, L. K.; Flamee, S.; Zhao, Q.; Vantomme, A.; Hens, Z. Less is More. Cation Exchange and the Chemistry of the Nanocrystal Surface. *ACS Nano* **2014**, *8*, 7948−7957.
(53) Veamatahau, A.; Jiang, B.; Seifert, T.; Makuta, S.; Latham, K.; Kanehara, M.; Teranishi, T.; Tachibana, Y. Origin of Surface Trap States in CdS Quantum Dots: Relationship Between Size Dependent Photoluminescence and Sulfur Vacancy Trap States. *Phys. Chem. Chem. Phys.* **2015**, *17*, 2850−2858.
(54) Tang, J.; Gao, B.; Pan, J.; Chen, L.; Zhao, Z.; Shen, S.; Guo, J.; Au, C.; Yin, S. CdS Nanorods Anchored with CoS_2 Nanoparticles for Enhanced Photocatalytic Hydrogen Production. *Appl. Catal., A* **2019**, *588*, No. 117281.
(55) Pan, J.; Shen, S.; Chen, L.; Au, C.; Yin, S. Core−Shell Photoanodes for Photoelectrochemical Water Oxidation. *Adv. Funct. Mater.* **2021**, *31*, No. 2104269.
(56) Pan, J.; Wang, B.; Wang, J.; Ding, H.; Zhou, W.; Liu, X.; Zhang, J.; Shen, S.; Guo, J.; Chen, L. Activity and Stability Boosting of an Oxygen-Vacancy-Rich $BiVO_4$ Photoanode by NiFe-MOFs Thin Layer for Water Oxidation. *Angew. Chem., Int. Ed.* **2021**, *133*, 1453−1460.
(57) Weng, B.; Qi, M.; Han, C.; Tang, Z.; Xu, Y. Photocorrosion Inhibition of Semiconductor-Based Photocatalysts: Basic Principle, Current Development, and Future Perspective. *ACS Catal.* **2019**, *9*, 4642−4687.
(58) Buehler, N.; Meier, K.; Reber, J. F. Photochemical Hydrogen Production with Cadmium Sulfide Suspensions. *J. Phys. Chem.* **1984**, *88*, 3261−3268.

https://doi.org/10.1021/acsanm.1c03997
ACS Appl. Nano Mater. 2022, 5, 2293−2304